



Gravity Investigation of Saturn's Inner System with the Innovative Skimmer Concept

Marzia Parisi¹ , Mar Vaquero¹, Matthew M. Hedman², and Matthew S. Tiscareno³¹Jet Propulsion Laboratory, California Institute of Technology, Pasadena, CA 91109, USA²Department of Physics, University of Idaho, Moscow, ID 83844, USA³SETI Institute, Mountain View, CA 94043, USA

Received 2021 October 13; revised 2021 December 28; accepted 2021 December 29; published 2022 January 25

Abstract

We present an in-depth feasibility study of innovative gravity science measurements of Saturn's inner system, which explores the different regions of the rings, the innermost moons, and the planet itself. The study is enabled by the novel Skimmer concept, where the spacecraft grazes repeatedly the rings over multiple passes. Because of the spacecraft's proximity to the rings, the experiment allows for the determination of their radial density distribution with unprecedented accuracy. These observations are especially important for the B and F rings, whose masses are not well constrained. During the closest approaches to Saturn, the spacecraft is sensitive to its tidal perturbations measured by the Love number k_{22} , which holds key information about the interior structure of the planet. The orbit geometry also allows for close flybys of icy moons not explored by the Cassini mission from a gravity perspective. Specifically, we focus on the measurements of Mimas's tidal perturbations, indicative of the presence of a submerged ocean under the icy surface. We perform precise numerical simulations of the gravity experiment and provide an account of the expected accuracies by means of a covariance analysis. The results are based on two trajectories of the Skimmer class which differ by altitude over the rings, proximity to Saturn, and number of passes. We find that the masses of the outer-ring regions are determined to better than 0.10 Mimas masses, with the case consisting of fewer but closer ring overflights generally yielding better accuracies. The 3σ uncertainty derived for Mimas's k_2 is 0.02, after six close equatorial flybys.

Unified Astronomy Thesaurus concepts: [Saturn \(1426\)](#); [Saturnian satellites \(1427\)](#); [Planetary rings \(1254\)](#); [Gravitational fields \(667\)](#)

1. Introduction

Saturn's inner system is a unique place in the solar system and a natural laboratory for the study of planetary formation and evolution (Murray & French 2018). With the emergence of ring seismology in the last decades (Marley & Porco 1993; Hedman & Nicholson 2013; Fuller 2014), it has become evident that the interior structure of planets and the dynamics of rings and inner satellites are inextricably interconnected. The observation of their interactions provides us with clues as to how a system arose and evolved (Mankovich 2020). The generative mechanisms between small inner bodies and some regions of the planetary rings have been extensively studied, as have their resonant relationships (Charnoz et al. 2005; Hedman et al. 2018). However, many questions relating to the material transport among the different regions of the rings are still largely unanswered (Tiscareno et al. 2021).

The Cassini mission provided a large amount of ring observations from several instruments (Colwell et al. 2009; Cuzzi et al. 2018), for the study of their dynamics, structure, and interaction with Saturn and its icy moons. The spacecraft performed observations of gravity and density waves rippling through the rings in connection to Saturnian seismic events and internal oscillations. Such observations have been related to measurements of the ring surface density at specific locations in the A, B, and C rings (Tiscareno et al. 2007; Hedman & Nicholson 2016, 2013), characterized by varying accuracy. The observations were extremely localized and could not provide a

global picture of the ring density distribution in the radial direction, particularly for the most massive B ring and the thin and active F ring, the latter hosting several kilometer-sized shepherd moons.

During the Cassini Grand Finale, the spacecraft flew between the rings and the upper atmosphere of Saturn, providing an opportunity for the independent measurement of the planet's oblateness and total mass of the rings by means of radiometric gravity measurements. Using precise Doppler tracking of the Cassini spacecraft, the total mass of the rings was estimated at about 0.41 times the mass of Mimas (Iess et al. 2019), with a relative formal uncertainty of about 32% (1σ). The estimate of the ring mass was, in turn, connected to the age of the rings, leading to the conclusion that they might be younger than previously thought (Iess et al. 2019). Localized estimation of the mass in specific regions of the rings could not be achieved because of the orbit geometry, as the concentric rings exerted an acceleration on the spacecraft from the same direction, rendering the decoupling of the gravitational pulls challenging when flying steeply through the gap between the rings and the planet for hazard avoidance (Seal & Buffington 2009). As opposed to the density wave observations, the gravity measurements carried out by Cassini provided a global measurement of the ring mass but lacked the necessary localization for providing a radial map of ring density.

Measuring the radial mass density distribution of the rings with the required accuracy would address outstanding questions and open up a whole new class of models for the formation and evolution of Saturn's inner system (Cuzzi & Estrada 1998; Estrada et al. 2015, 2018). A mission designed after the novel Skimmer concept (Vaquero et al. 2019;



Original content from this work may be used under the terms of the [Creative Commons Attribution 4.0 licence](#). Any further distribution of this work must maintain attribution to the author(s) and the title of the work, journal citation and DOI.

Tiscareno et al. 2021) would provide an opportunity to carry out close gravity measurements of the rings, allowing for accurate localized characterization of the disk system. The Skimmer’s equatorial trajectory is optimized for the observation of Saturn’s rings at altitudes lower than 100 km over the disk plane as well as several flybys of Mimas, Enceladus, Rhea, Dione, and Titan. Flybys of the latter are used for trajectory optimization purposes, as well.

Mimas is the innermost of Saturn’s mid-sized moons and the smallest, with a mean diameter just short of 400 km (Roatsch et al. 2009). Its external appearance is heavily cratered, with no evidence of geological activity (Neveu & Rhoden 2017). The moon is mostly recognizable from the presence of the Herschel crater, whose diameter is about a third of that of the moon, and likely resulted from a large impact (Dermott & Thomas 1988). The small moon is often compared to its neighbor Enceladus, which is slightly larger and more distant from Saturn. Enceladus is geologically very active with visible water vapor plumes emerging from the south pole and a hidden global liquid ocean underneath the striped surface (Iess et al. 2014; Thomas et al. 2016). In contrast, despite tidal forces acting on Mimas that are predicted to reach levels about 30 times larger than for Enceladus (due to the orbit eccentricity and proximity to Saturn), the moon appears geologically inactive (Neveu & Rhoden 2017). This condition is known as the Enceladus–Mimas paradox. Precise measurements of the moon’s gravity field could shed light on the origins of such visible differences. The Cassini Image Science Subsystem instrument (ISS) was able to observe and detect librations of its icy shell and concluded that their magnitude was twice the predicted value (Tajeddine et al. 2014). The discrepancy was explained with an interior that is either nonhydrostatic or hiding a liquid ocean underneath the thick shell. The presence of a liquid reservoir could be confirmed by gravity measurements of its gravity field and tidal potential, closely related to the inner structure of the moon, similarly to what was done for Titan (Iess et al. 2012) and Enceladus (Iess et al. 2014). In addition to closely flying over the rings of Saturn, the Skimmer trajectory provides an opportunity to systematically fly close to the surface of Mimas so as to obtain additional information about its internal structure.

On this basis, we performed a feasibility study for this class of observations through precise numerical simulations and a covariance analysis of the achievable estimation accuracies. In this scenario, the recovered formal uncertainties are generally optimistic, with a strong dependence on the data weight, which is simulated on the basis of expected measurement noise and on the geometry of the trajectory. However, a covariance analysis is indicative of the potential of proposed gravity measurements. The innovative trajectory design is what enables the science investigation described in this paper, which is divided as follows. In Section 2 we present the Skimmer trajectory and describe the characteristics that make it optimal for the science questions we wish to address. In Section 3 we describe the simulation setup, including the frequency of the observations, coverage from the Earth station, and instrumentation details. In Section 4 we present the results of our analyses, for both proposed scenarios, in terms of radial distribution of the rings’ mass, and Saturn’s and Mimas’s tidal perturbations. Lastly, Section 5 presents a discussion of the results and conclusions.

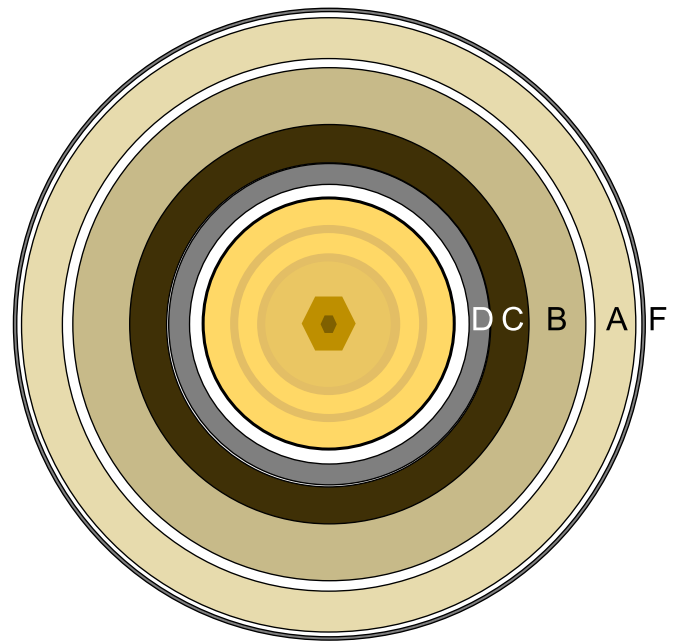


Figure 1. Sketch of Saturn’s D, C, B, A, and F rings, as seen from the planet’s north pole. These regions extend from about 1.1 to 2.3 Saturn’s radii. While most of the ring mass is concentrated in the A, B, and C regions, the F ring hosts a population of small moons.

Table 1

Radial Extensions of the Different Ring Regions Considered in this Study (Colwell et al. 2009; Cuzzi et al. 2018)

Name	Inner Radius (km)	Width (km)	
D ring	66,900	7,610	
C ring	74,658	17,317	
B ring	B I	91,975	7,025
	B II	99,000	5,500
	B III	104,500	5,500
	B IV	110,000	6,800
	B V	116,800	707
A ring	122,340	14,440	
F ring	139,826	30–500	

Note. There are two major gaps between rings B and A and A and F (both of a few thousand kilometers), the Cassini Division and the Roche Division, respectively.

2. Saturn’s Rings and the Skimmer Trajectory

Figure 1 shows a simplified illustration of Saturn’s D, C, B, A, and F rings, extending outwardly to roughly 2.3 times Saturn’s mean radius. The width of the rings are reported in Table 1. Of these, most of the mass in the ring system lies in the A, B, and C rings, while the F ring likely contains a population of small moons. Density waves have been observed in the A, B, and C rings (Tiscareno et al. 2007; Hedman & Nicholson 2016, 2013), the first two being the densest regions of Saturn’s ring system and the most systematically observed by the Cassini mission. The B ring, which is Saturn’s densest and widest ring, is further divided into subregions BI, BII, BIII, BIV, and BV, as described in Table 1. The A, B, and C rings are characterized by a vertical thickness between 5 and 30 m

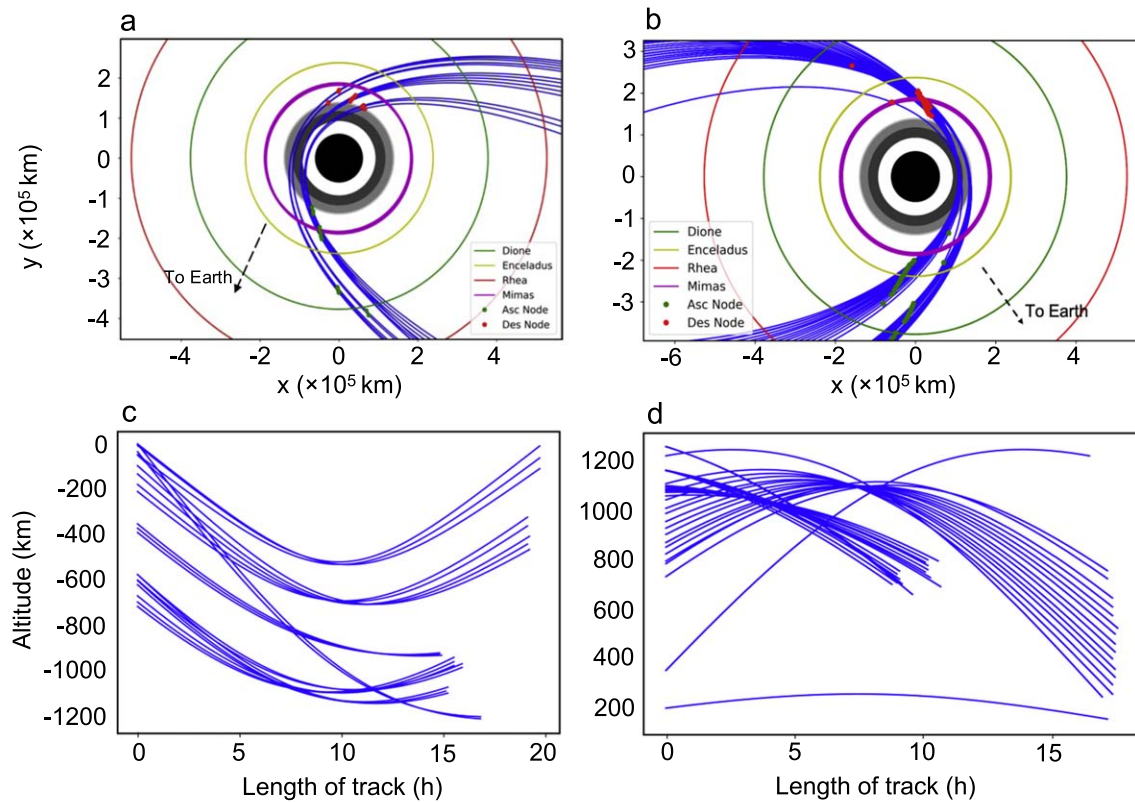


Figure 2. Trajectory design for Scenario 1 (left) and Scenario 2 (right). Panels (a) and (b) show the view of the ring overflights (in blue) from the orbital pole, for a total of 21 and 32 passes, respectively, grazing different regions of Saturn’s rings. The orbits of the innermost moons are also displayed. The reference frame is Saturn’s mean equator. Panels (c) and (d) show the orbital altitude of the spacecraft with respect to the ring plane throughout the duration of the track, referenced to the beginning of pass for each ring overflight. The beginning and end of each pass mark the time period for which the spacecraft position is inside the F ring. The altitude is negative in panel (c) because the passes occur below the ring plane, while it is positive in panel (d) as passes occur above the ring plane.

(Tiscareno et al. 2007; Cuzzi et al. 2018), which is orders of magnitude smaller than their extension in the ring plane. The region surrounding the outer A and F rings also contains two known moons, Prometheus and Pandora, and may contain moonlets with sizes ranging from 8 to 180 km.

The Skimmer mission concept comprises an entire class of trajectories that allow the spacecraft to fly repeatedly over planetary rings at close range (Figure 2). The space of trajectory design that maximizes the scientific return of the ring observation has been extensively discussed in Vaquero et al. (2019) in terms of distance, relative velocity with respect to the rings, and number of passes. The spacecraft performs 3–4 passes per month over the major regions of Saturn’s rings. Each pass lasts several hours with low flyover velocities ($\sim 10 \text{ km s}^{-1}$). The trajectory is fueled by an optimized sequence of Titan flybys, which requires minimal use of propellant and considerably extends the mission duration. Furthermore, because of the equatorial character and eccentricity of the trajectory, it is possible to repurpose and explicitly target the naturally occurring flybys of the inner moons, so as to reach very low altitudes above the icy surfaces and the desired ground track geometry. In this investigation we focus on flybys of Mimas for the detection of hidden liquid reservoirs underneath the moon’s icy crust.

We consider two different scenarios based on the Skimmer concept. The differences pertain mainly to the orbital geometry for the close flybys of the rings. In Scenario 1 (Figures 2(a), (c)), the spacecraft flies over the rings and close to the planet 21 times for a total mission duration of 8 months, sweeping the

different regions of the rings within 3–5 hr. The spacecraft velocity reaches radial values of up to 15 km s^{-1} and tangential velocities of up to 8 km s^{-1} . A key feature is represented by the low altitudes reached by the spacecraft over the ring plane, with minima well below 100 km when closer to the outer edge of the rings (F ring). This geometry is very favorable for gravity observations, since the measurable gravitational potential of uniform disks is proportional to r^{-3} , where r is the distance from the ring plane (Lass & Blitzer 1983). Thus, the closer the spacecraft flies to the rings, the stronger the gravitational acceleration exerted on the spacecraft and the larger the Doppler shift on the radio signal.

In Scenario 2 (Figures 2(b), (d)), the number of ring overflights and Saturn pericenters is increased to 32, for an overall mission duration of 11 months. The spacecraft altitude over the ring plane is higher on average than for Scenario 1, with minimum values around 200 km. The comparison between the two scenarios is carried out to quantify the trade-off between the number of passes, which in general improves the accuracies of gravity measurements, and the altitude increase, which has the opposite effect. Both scenarios occur at epochs between late 2034 to mid-2035, based on a hypothetical launch date in the late 2020s.

3. Simulation Setup of the Gravity Experiment

3.1. Data Simulation and Instrument Noise

The simulation process described in this section, from trajectory integration and synthetic data generation, to the

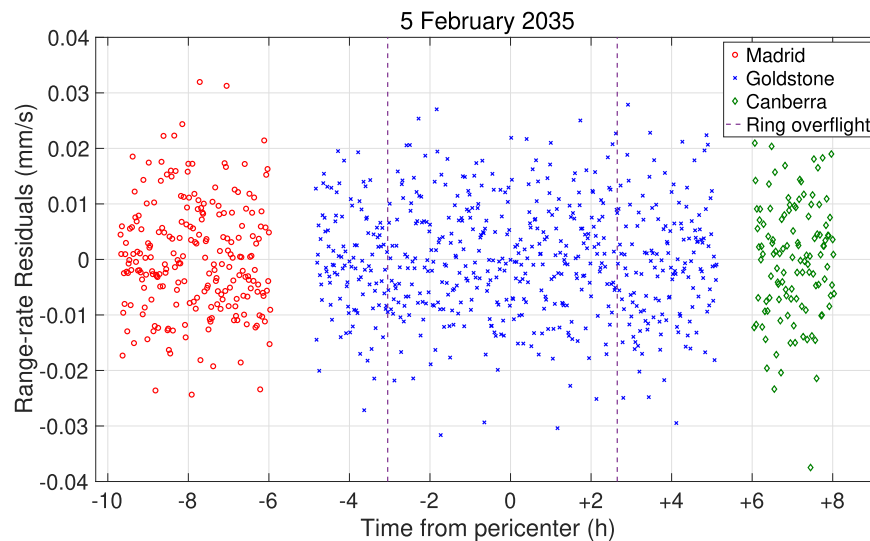


Figure 3. Example of simulated range-rate residuals from a tracking pass of the spacecraft by NASA’s Deep Space Network antennas at 60 s integration time. The ring overflight (dashed lines) is visible from the Goldstone complex for about 8 hr around closest approach to Saturn. The (one-way) noise rms is 0.010 mm s^{-1} .

assessment of formal parameter uncertainties, was carried out using the Jet Propulsion Laboratory’s (JPL) Mission Analysis, Operations, and Navigation Toolkit Environment (MONTE; Evans et al. 2018). We assume that the spacecraft is orbiting Saturn while maintaining almost continuous radio links with the ground stations of NASA’s Deep Space Network, for at least ± 4 hr centered around closest approach to Saturn (Figure 2). The choice of this time interval ensures the inclusion of the ring overflights. We also assume that the spacecraft is equipped with X- and Ka-band translators, capable of establishing two-way coherent radio links (X/X and Ka/Ka) with ground stations through the onboard High-Gain Antenna. The instrumentation considered in this work is similar to the equipment on board NASA’s Juno mission (Asmar et al. 2017). This configuration allows for precise Doppler tracking of the spacecraft, and for the compensation of up to 75% of dispersive plasma noise (Mariotti & Tortora 2013). The main observable of planetary gravity experiments is the two-way spacecraft range-rate, which measures the spacecraft velocity fluctuations at large interplanetary distances. We assume that the synthetic range-rate observables generated for the numerical simulations are characterized by one-way accuracies between 0.005 and 0.010 mm s^{-1} at 60 s integration time, in accordance with recent Juno gravity measurements (Durante et al. 2020).

There are several factors that need to be considered when designing a gravity experiment. A major concern is the visibility of the spacecraft from the ground stations. The line of sight between the spacecraft and the Earth, which varies depending on the epoch of the observations, must be free of interjecting objects during radio communications. For Scenarios 1 and 2, the variations of the Skimmer trajectory have been designed so that the Earth is never occulted by the rings. Another factor that must be considered is possible occultations of the Earth by Saturn along the spacecraft trajectory. In the two scenarios analyzed in this work, the spacecraft’s closest approaches to Saturn, and by extension the ring overflights, are always visible from the Earth (Figures 2(a), (b)).

At present, only one 34 m deep space antenna (DSS 25) of the Goldstone complex is capable of uplinking to the spacecraft in the Ka-band. For our simulations we assume that by year 2034, the Canberra and Madrid complexes will be equipped

with at least one large-dish antenna capable of establishing Ka-band uplinks with interplanetary spacecraft. The minimum station elevation angle was set to 10° above the horizon in order to avoid large errors in the path delay due to the Earth’s troposphere. Figure 3 shows an example of simulated range-rate data for one tracking pass of the spacecraft during a ring overflight. The gaps visible in the Doppler data are due to the station visibility from Earth, which depends on Saturn’s and the Earth’s seasons, and are also influenced by the choice of the cut-off elevation chosen to limit troposphere noise. The synthetic range-rate residuals were generated assuming that the dynamical model surrounding the spacecraft is perfectly known, therefore including only Gaussian noise on the measurements. This approach, known as covariance analysis, is used to predict the formal uncertainties on the estimated physical parameters of interest, through precise trajectory reconstruction.

3.2. Dynamical Model

As the spacecraft moves through the planetary surroundings, its trajectory is affected by gravitational and nongravitational forces, which cause variations in its velocity along the line of sight. In order to integrate the spacecraft trajectory as realistically as possible starting from given initial conditions, one needs to define a dynamical model in the MONTE environment (Evans et al. 2018), which includes all known accelerations acting on the spacecraft. The gravitational accelerations considered include the following: Saturn’s gravitational pull, along with gravity perturbations from the Sun and the other planets; Saturn’s spin axis position from the latest IAU model (Archinal et al. 2018), and zonal harmonic coefficients from degree 2 to 12 (Iess et al. 2019); Saturn’s degree-2 tidal perturbation, with a nominal value for k_{22} of 0.390 (Lainey et al. 2017); and the gravitational pull from Saturn’s icy satellites, as well as those from the shepherd moons of the F ring, Pandora, and Prometheus (Jacobson 2016). The position of the planets and the satellites in the Saturnian system are reported in the JPL planetary ephemeris DE440 (Park et al. 2021) and satellite ephemeris SAT393 and SAT427 (Jacobson 2016, 2020). The nongravitational effects include the

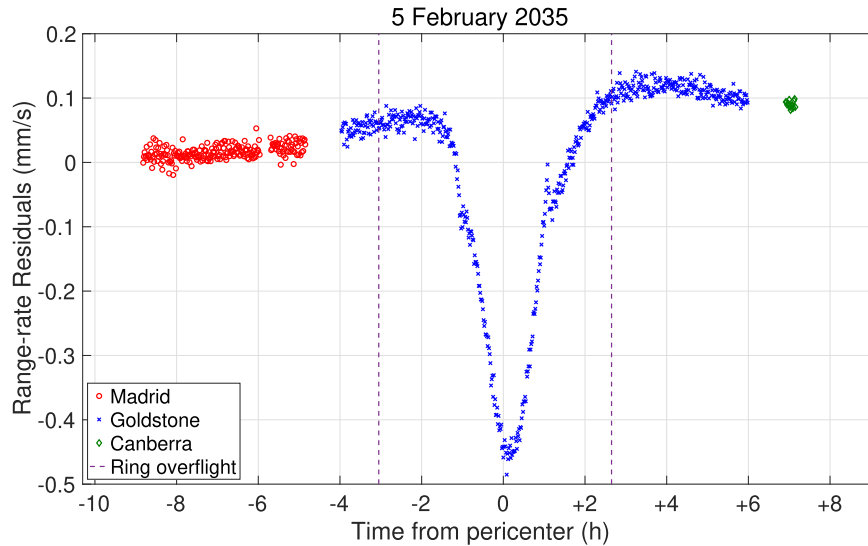


Figure 4. The range-rate residuals in Figure 3 are perturbed in this plot by changing the mass of one of the ring regions. The signatures during the ring overflight and the noise rms of the perturbed data (0.131 mm s^{-1}) are larger than the noise rms of flat residuals.

solar radiation pressure, Saturn’s albedo and thermal emission, which require information about the spacecraft’s components. The probe is modeled after the shape of the Cassini spacecraft. The structure is composed of elementary geometrical components, such as plates, cylinders, and dishes. This approach is an approximation, and the uncertainties in the characteristics and properties of the components and materials are taken into account by estimating scale factors. These accelerations can, in principle, cause detectable Doppler shifts on the radio signals received at Earth’s stations, related to the spacecraft range-rate. We evaluated the magnitude of the albedo and thermal accelerations on the spacecraft from Saturn, for a typical ring pass. The results show that they are smaller than $10^{-13} \text{ km s}^{-2}$ at any given time. These levels are much lower than the typical smallest detectable accelerations for a state-of-the-art gravity experiment, usually of the order of $10^{-12} \text{ km s}^{-2}$. By taking into account the albedo of the rings as well as that of the planet, we found an average acceleration that is about 40% larger than the case without the rings, still well below the detectability threshold. The additional effect from the rings’ thermal emission is negligible, as well.

The vertical extension (or thickness) of the rings is about 10^{-8} times smaller than their horizontal extension (or width). For this reason, we modeled Saturn’s nine ring regions considered in this work using disk mass concentrations, where one dimension is negligible compared to the other two. The values in Table 1 were used to define an inner radius and thickness. We assigned a mass for each disk anomaly corresponding to a different region, using approximations based on previous estimations (Tiscareno et al. 2007; Hedman & Nicholson 2013, 2016; Iess et al. 2019). The masses of the rings are central parameters to our analysis, therefore we are interested in evaluating the effect on the Doppler data of perturbing the mass of one or more regions. Figure 4 shows the Doppler residuals for the same pass of Figure 3, after the mass of the BV region of the B ring was perturbed by 0.10 Mimas masses. All other parameters defining the dynamical model are kept unperturbed. The plot shows that the signature introduced on the Doppler data is well above the noise level (0.010 mm s^{-1}), and indicates that small deviations from the nominal values are likely detectable.

The nonmonopole gravity field of Mimas is unknown, due to the lack of close Cassini flybys of the icy moons. However, the values for the degree-2 gravity field have been predicted using the satellite’s topography as reconstructed using limb profiles (Nimmo et al. 2011), which were used as nominal values for simulation purposes. The higher-degree gravity field is instead set to zero. The degree-2 tidal Love number is also undetermined for Mimas, with a central value that varies greatly depending on the interior structure and presence of a liquid ocean (Neveu & Rhoden 2017). Since the results pertaining to the formal uncertainties on the estimated parameters are not affected by the choice of the nominal values in the dynamical model, we arbitrarily assumed $k_2 = 0.2$ for Mimas. The rotation parameters for the small moon were also obtained from the IAU report (Archinal et al. 2018), which are consistent with its tidally locked rotation rate.

3.3. Estimation Process

After defining the dynamical model, we simulate the spacecraft Doppler tracking data for all ring passes (21 or 32) and Mimas flybys (six in total). These synthetic observables are compared to computed observables which are calculated starting from the current knowledge of the dynamical model. In the context of real gravity experiments, these differences are used to improve the knowledge of physical parameters such as planetary gravity fields and mass anomalies. In the context of numerical simulations these differences usually contain the measurement noise (covariance analysis), and are used to predict the estimation accuracies on such parameters.

Each simulation event is contained in an arc of 24 hr duration, centered about the 8 hr ring pass of continuous tracking. The range-rate residuals from all arcs are combined in a multiarc square-root information filter for the estimation of parameters of interest (Durante et al. 2020; Parisi et al. 2020). The simulation setup allows for the estimation of parameters that are independent for each arc, called local in Table 2. In this work these are as follows: the spacecraft state vector (position and velocity), as well as the albedo, thermal, and solar pressure scale factors. The latter are uncertain because they depend on the spacecraft geometry as well as its optical and thermal

Table 2
List of Estimated Local and Global Parameters

	Estimated Parameters
Local	State vector ($\times 6$) Albedo scale factor ($\times 1$) Thermal emission scale factor ($\times 1$) Solar radiation pressure scale factor ($\times 1$) Random accelerations ($\times 36$)
Global	Saturn system barycenter Gm ($\times 1$) Saturn's R.A. (degrees 0, 1) ($\times 2$) Saturn's decl. (degrees 0, 1) ($\times 2$) Saturn's $J_2 - J_{20}$ ($\times 19$) Saturn's degree-2 tesseral field ($\times 4$) Real part of Saturn's k_{22} ($\times 1$) Masses of the ring regions ($\times 9$) Prometheus's Gm ($\times 1$) Prometheus's state vector ($\times 6$) Pandora's Gm ($\times 1$) Pandora's state vector ($\times 6$) Mimas's Gm ($\times 1$) Mimas's degree-3 field ($\times 12$) Mimas's k_2 ($\times 1$) Mimass's state vector ($\times 6$)

properties, which are not always perfectly known. Oppositely, some parameters are estimated globally for all arcs. These include the mass of Saturn's system barycenter, Saturn's pole position (constant and linear terms), Saturn's zonal gravity field up to degree-20 and degree-2 tesseral field, the real part of Saturn's tidal Love number k_{22} , Mimas's mass, Mimas's degree-3 gravity field, and Mimas's Love number k_2 . This category also includes the mass of the different ring regions and the two shepherd moons of the F ring, Pandora, and Prometheus. The rings are modeled as nine disk mass concentrations (one for each region in Table 1), characterized by an inner radius, an outer radius, and a mass. The gravity experiment will also improve the knowledge of the state of Saturn's inner satellites, parameters that are estimated as well but not discussed. The a priori uncertainties on all parameters are set very loose, which means that these quantities are unconstrained.

Iess et al. (2019) provided a global solution for the gravity field of Saturn and ring mass from the Cassini Grand Finale. One of their main findings was the presence of axially asymmetric accelerations, which were strongly dependent on the single pass. Because the accelerations were observed to peak at closest approach to Saturn, and decreased with distance, it can be assumed that they are gravitational in nature, due perhaps to longitudinal atmospheric effects or even internal oscillations (Iess et al. 2019). In a recent work, Markham et al. (2020) interpreted the unknown accelerations as normal modes. In this case, the accelerations would also largely decrease as the spacecraft moves away from the planet. However, determining the precise nature of these accelerations with the limited Cassini data set is very challenging. In order to reduce the range-rate data to the noise level, the preferred solution by Iess et al. (2019) had to include arc-dependent random constant accelerations for 2 hr around closest approach to Saturn. The three components of the accelerations were allowed to vary with a timescale of 10 minutes. The a priori constraint for these short-scale constant accelerations was $4 \times 10^{-7} \text{ m s}^{-2}$. Similarly, in this study we take into account the presence of

unknown longitudinal effects by estimating empirical accelerations (three components) as local parameters, also within 1 hr of closest approach, with the same 10 minute variability and a priori uncertainties as Iess et al. (2019). The latter value is large enough to absorb the unknown longitudinal or temporal effects, according to Iess et al. (2019). However, the estimated accelerations are not considered unconstrained like the other parameters (e.g., the zonal harmonics have a priori uncertainties of 1). If the accelerations were left unconstrained, the data at closest approach would be deweighted to the point of not carrying significant information. If indeed the unknown accelerations are of a gravitational nature, we expect the gravity field of Saturn to affect the Skimmer trajectory less strongly than for the Cassini observations, as in this case the closest approaches to Saturn occur at a distance of about 10,000 km, against 2600–3900 km for the Cassini Grand Finale (Iess et al. 2019). Therefore, we consider the inclusion of large random accelerations rather conservative. Table 2 reports the complete list of estimated parameters.

4. Results

4.1. Scenario 1

The results of the Skimmer gravity experiment for Scenario 1 are summarized in this section, in terms of formal uncertainties on the estimated parameters. Figure 5 shows distinct solutions with (dashed lines) and without (solid lines) the use of empirical accelerations. We express all the results in terms of Mimas masses, where $m_m = 3.7496 \times 10^{19} \text{ kg}$ or $Gm_m = 2.5026 \text{ km}^3 \text{ s}^{-2}$ (Iess et al. 2019).

We start by discussing the determination of the mass of the C ring, which extends between 74,660 and 92,000 km from the center of the planet. This region is the farthest from the spacecraft during the flybys (Figure 2(c)), therefore we do not expect to retrieve its mass with remarkable accuracy. Our simulations show a 3σ uncertainty of about 7×10^{-2} Mimas masses at the end of the 21 passes, which increases to 2×10^{-1} Mimas masses with the use of random accelerations (Figure 5(a)). The increase in the uncertainties are due to the effective deweighting of the Doppler data around perijove from random accelerations. The retrieved uncertainties are larger than the most recent estimated value for the mass of the C ring (Hedman & Nicholson 2014), therefore confirming that the spacecraft is too far away to be sensitive to the subtle perturbations induced by this region. As we move away from the center of the planet, the spacecraft is bound to fly closer to the ring plane. As a result, the masses of the separate B-ring regions (92,000–117,580 km) can be determined with 3σ uncertainties between 9×10^{-4} and 3×10^{-2} Mimas masses (from BV to BI), while these increase to a range between 4×10^{-3} and 6×10^{-2} Mimas masses when using constant accelerations (Figure 5(b)). Similar results are found for the A ring (122,170–136,775 km), with 3σ uncertainties spanning between 4×10^{-3} and 5×10^{-3} Mimas masses (Figure 5(c)).

The F ring is located at the outer edge of the system and is only 500 km wide. This is also the region most closely observed by the spacecraft (Figures 2(c), (d)), and whose density is not well known. The estimated 3σ accuracy for its azimuthal mean mass is 6×10^{-8} Mimas masses at the end of mission (Figure 5(d)), which corresponds to a single ice-rich object with a radius of only $\sim 1 \text{ km}$.

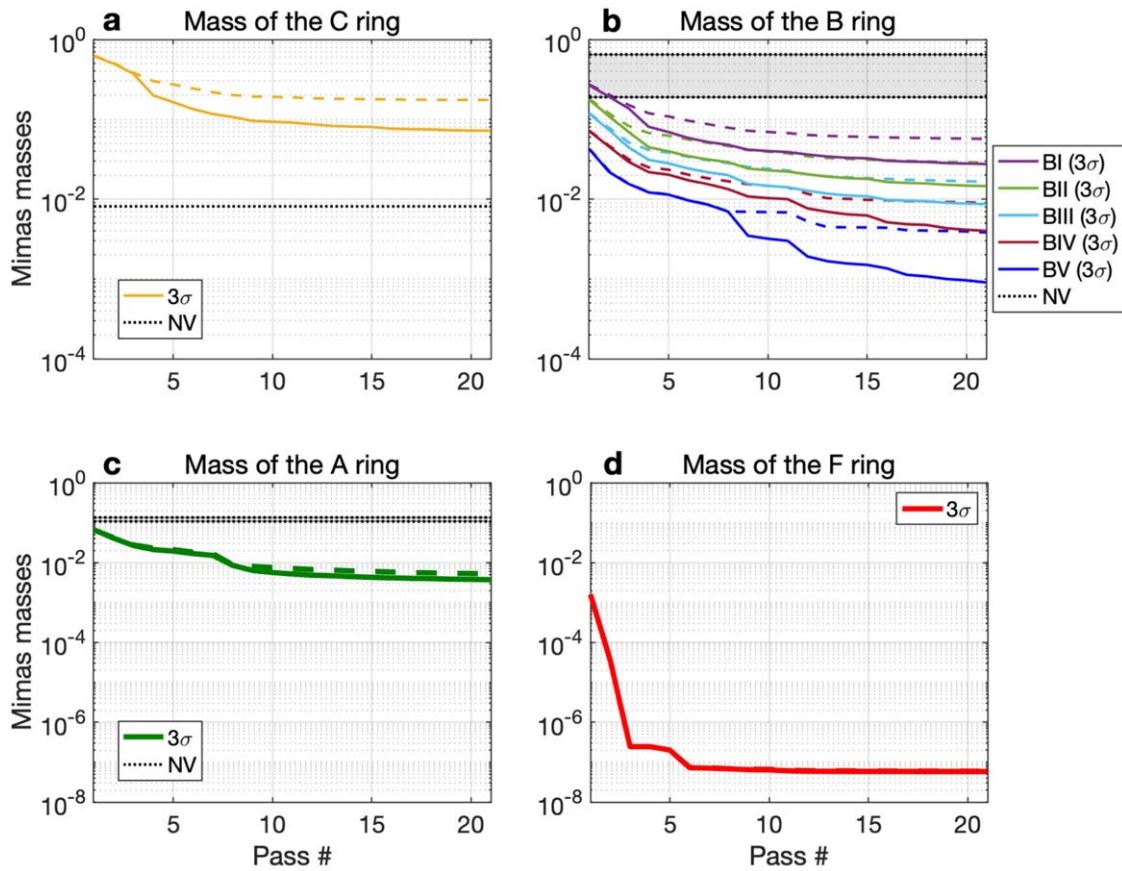


Figure 5. Results of the gravity experiment simulations for Scenario 1, in terms of the mass of the C (a), B (b), A (c), and F (d) rings. The plots show the uncertainties (3σ) considering a purely zonal field for Saturn (solid lines), or considering longitudinal/temporal variations of the gravity field absorbed by constant accelerations around closest approach (dashed lines). The uncertainties are a function of the number of passes and generally improve with mission duration. The black dotted lines or gray shaded areas show the range of nominal values (NV) for the masses of the different rings (Tiscareno et al. 2007; Hedman & Nicholson 2014, 2016), except for the F ring, for which there is no reliable mass estimate.

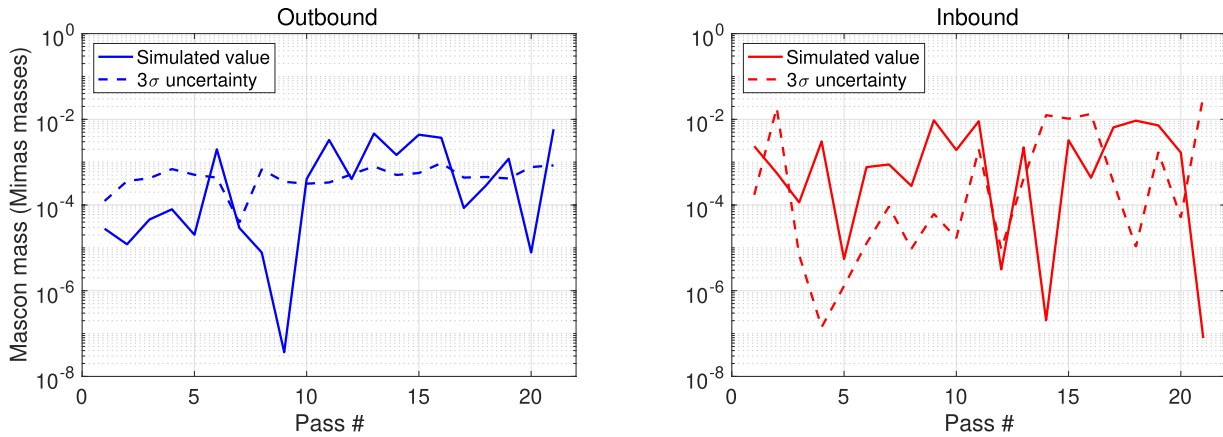


Figure 6. Simulated values (solid lines) and retrieved 3σ uncertainties (dashed line) for the outbound and inbound mass concentrations placed in the F ring.

Hundreds to thousands of such objects are expected to exist in the F ring (Barbara & Esposito 2002; Esposito et al. 2008; Murray & French 2018), therefore we are also interested in the determination of the longitudinal variations of the ring mass along each overflight (Cuzzi et al. 2018). In order to determine these fluctuations, we resort to using mass concentrations, or mascons, which are widely used to model the gravitational effects of local density anomalies (Parisi et al. 2021). For each F-ring overflight, we placed a flat-disk mascon, of radius 250 km, over the ring region most closely observed by the

spacecraft. Since each pass includes two F-ring overflights (Figure 2(a)), we placed a total of 42 mascons (for the 21 passes of Scenario 1), along the F ring and at different longitudes. By estimating the Gm of each mascon as local parameters, we found that the local mass variations of the F ring can be estimated with 3σ accuracies between 2×10^{-7} and 3×10^{-2} Mimas masses, depending on the arc considered. Figure 6 shows the simulated values (solid lines) for the outbound and inbound mass concentrations for each of the 21 passes of Scenario 1. The simulated values were randomly

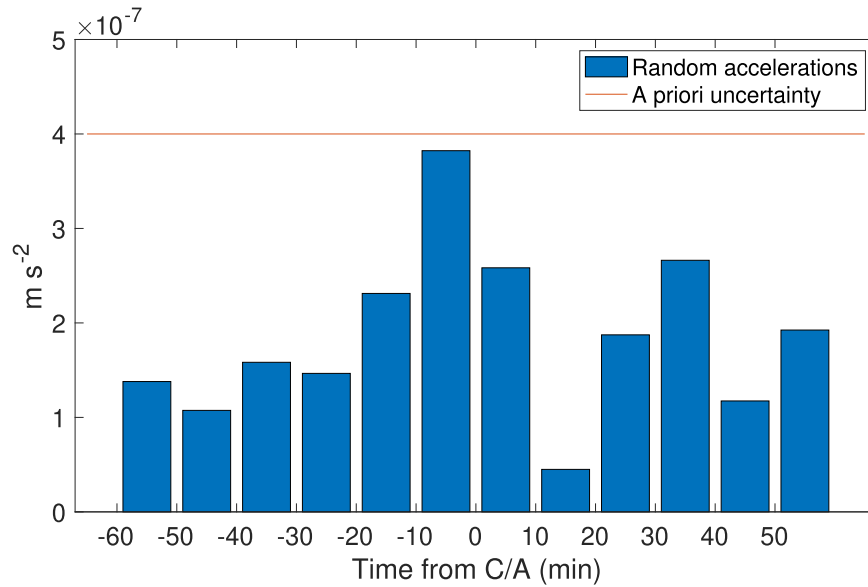


Figure 7. Time series of random accelerations for one of the ring passes of Scenario 1 (#2). The timeframe is 2 hr around closest approach to Saturn. The a priori uncertainty value was chosen according to Cassini gravity science results (Iess et al. 2019).

assigned between the predicted mass for a 1 km radius object ($\sim 10^{-7}$ Mimas masses) and the estimated mass for Pandora and Prometheus ($< 10^{-2}$ Mimas masses). The plots also show the corresponding 3σ uncertainties on the local parameters (dashed lines) as recovered with numerical simulations. This approach allows for the retrieval of a coarse longitudinal map of the density profile within the F ring, although not very refined as the accuracies are in some cases comparable or higher than the expected mass fluctuations.

The inclusion of random accelerations does not affect the results for the recovery of the F-ring mean mass or mass concentrations. The reason is that the accelerations are concentrated ± 1 hr around closest approach, while the F-ring overflights occur on average at least 1.5 hr before and after closest approach, therefore outside of the active acceleration range. We did not consider any mismodeling of the accelerations in our covariance analysis, as this is outside of the scope of this work. However, the unknown nature of these forces makes predicting their effect on the spacecraft trajectory quite difficult. Figure 7 shows the values of the random accelerations for one of the ring overflights (#2), as a function of time from closest approach. The parameter is allowed to vary every 10 minutes, while remaining constant in the selected time window (Durante et al. 2020). The accelerations cover 2 hr around closest approach, when the spacecraft is the most sensitive to fluctuations of the gravity field of Saturn.

Prometheus is characterized by an orbital semimajor axis around Saturn of 139,380 km and a mass previously determined at about 4×10^{-3} Mimas masses (Jacobson 2016). Our simulations predict a 3σ relative accuracy for its mass (Figure 8(a)) of better than 10% at the end of mission, because of two close encounters of the spacecraft with the moon at altitudes 5550 and 3490 km. The results do not vary with the use of constant accelerations. Pandora orbits Saturn with a semimajor axis of 141,720 km and a mass of about 4×10^{-3} Mimas masses, as well (Jacobson 2016). The 3σ measurement accuracy is around 2% at the end of mission (Figure 8(b)). The smaller uncertainty value depends on the proximity of the spacecraft to Pandora during the encounters with the small

moon at altitudes of 2780 and 3880 km. This occurs by chance, but it gives an indication of what is likely for any nominal tour. The results can be further improved if one decides to pursue closer targeted flybys of Prometheus and Pandora. The results take into account the large uncertainty in the position and velocity of the shepherd moons, by estimating the position of the small objects throughout the duration of the mission. Improving the ephemeris of such bodies is not the objective of this work, but rather, including the effect of the uncertainties on the retrieval of gravitational parameters of interest.

The focus of this study is the determination of the mass of the different ring regions. However, the equatorial nature of the Skimmer trajectory also allows us to consider a bonus science objective: the measurement of Saturn’s tidal Love number k_{22} . This parameter represents the temporal variations of the degree-2 gravity field of Saturn due to the satellites’ orbital motion around the planet. Despite the greater distance from the planet during the pericenters than for Cassini observations, our simulations indicate that one can determine Saturn’s k_{22} with a 3σ accuracy of about 0.027 without the use of constant accelerations (Figure 8(c)). Assuming that the central value is close to 0.390 (Lainey et al. 2017), this translates to a relative accuracy of about 7%. When using empirical accelerations, the 3σ uncertainty increases to about 0.150 or 38% relative uncertainty, likely too large to infer characteristics of the interior structure of Saturn. However, in order to take advantage of the large number of passes considered in this work and to better understand the nature of the longitudinal or temporal accelerations detected by the Cassini mission (Iess et al. 2019), the spacecraft would need to get as close as 2000–3000 km to the planet’s atmosphere, which might not be compatible with the Skimmer trajectory. Furthermore, we must note that our simulations were carried out assuming that Saturn’s tides are satellite independent, which implies that the Love numbers are invariant for all moons. One should consider that both the real and imaginary parts of Saturn’s k_{22} may differ for each satellite, instead, rendering the use of a satellite-dependent model necessary (Notaro et al. 2019; Wahl et al. 2020). The bulk of the tidal deformations are characterized by a

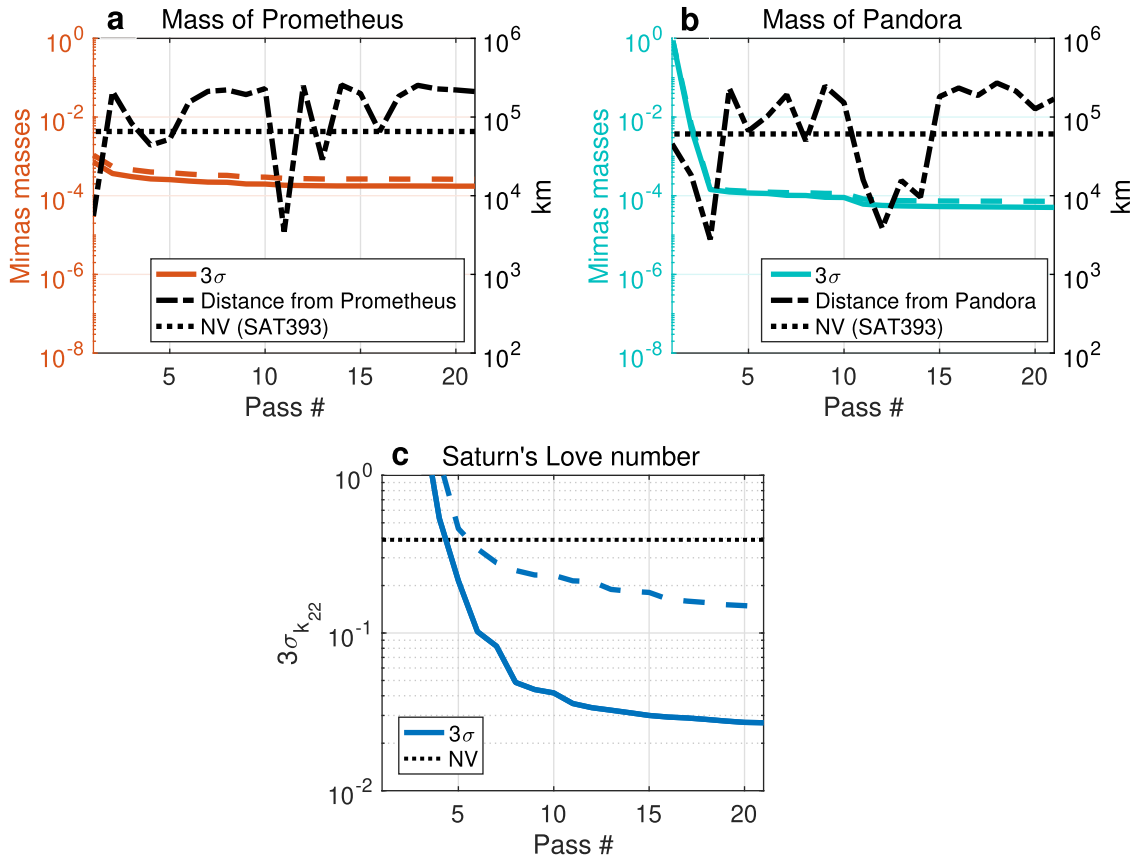


Figure 8. Results of the gravity experiment simulations for Scenario 1, in terms of the mass of Prometheus (a) and Pandora (b), and Saturn’s Love number (c). The plots show the uncertainties (3σ) considering a purely zonal field for Saturn (solid lines), or considering longitudinal/temporal variations of the gravity field absorbed by constant accelerations around closest approach (dashed lines). The black dashed-dotted lines in panels (a) and (b) show the distance of the spacecraft from the moon for each flyby under the nominal trajectory. Flybys at less than 10^4 km distance drive the accuracy of the measurement. Just by chance, the nominal trajectory has two such flybys for Prometheus and three for Pandora. The dotted lines represent the nominal values (NV) (Jacobson 2016; Lainey et al. 2017).

frequency consistent with Titan’s period, and if a significant lag angle between the tidal bulge raised by Titan and the radial position of the moon were found (Lainey et al. 2030), it would be necessary to estimate the imaginary part of Saturn’s k_{22} , as well. We calculated that this would degrade the uncertainty on the real part by about 40% on average, with the imaginary component characterized by a similar uncertainty.

4.2. Scenario 2

The trajectory design for this case comprises a larger number of ring overflights (32 in total), although at higher average altitudes above the ring plane (Figure 2(b)). By looking at this case, we determine the trade-off between the number of passes and altitude. In general, the results displayed in Figure 9 show that the altitude over the ring plane and the number of flybys both play an important role in the estimation process, and the optimal combination can be chosen considering these two balancing effects. In order to first study the impact of altitude only on the estimation accuracies, we consider the results obtained for Scenario 2 after 21 passes (out of a total of 32), which equates the number of overflights in Scenario 1. For instance, in the case of the determination of the mass of the C ring, the average altitude of the spacecraft increased from about 600 km in Scenario 1 to about 1000 km in Scenario 2. As a result, this parameter is undetermined in the latter case, as well, regardless of the number of passes (Figure 9(a)). Similarly, by comparing the results in the determination of the B-ring mass

after 21 passes in Figures 5(b) and 9(b), it emerges that altitude has a large impact on the estimation of the masses of the different regions (BI to BV). In particular, the mass of the BI ring is undetermined in Scenario 2, and the addition of passes 22–32 does not improve the estimated accuracy. The results pertaining to the end-of-mission estimation of the mass of the A ring do not change remarkably between the two scenarios (Figure 9(c)). After 21 passes, this parameter is determined with an uncertainty which is about twice as large as for Scenario 1, suggesting that the inclusion of passes 22–32 is necessary to reduce the uncertainty by a factor of 2. On the other hand, the predicted uncertainty in the estimation of the mass of the F ring is unvaried after about 10 passes, suggesting that the number of overflights included in Scenario 1 could potentially be sufficient to determine the parameters with the desired accuracy.

The masses of the shepherd moons are better determined in this case (relative accuracy $\sim 1\%$), due to the lower distance from the spacecraft during the fortuitous encounters with the moons (2360 and 850 km for Prometheus and 1170 km for Pandora; Figures 10(a), (b)). The results for Saturn’s k_{22} estimation are virtually unvaried in Scenario 2, with a final uncertainty (3σ) of 0.023 (0.179) without (with) the use of stochastic accelerations (Figure 10(c)).

Table 3 compares the results obtained during the ring-centered portion of the gravity experiments, in terms of formal uncertainties on the estimated parameters, using the two

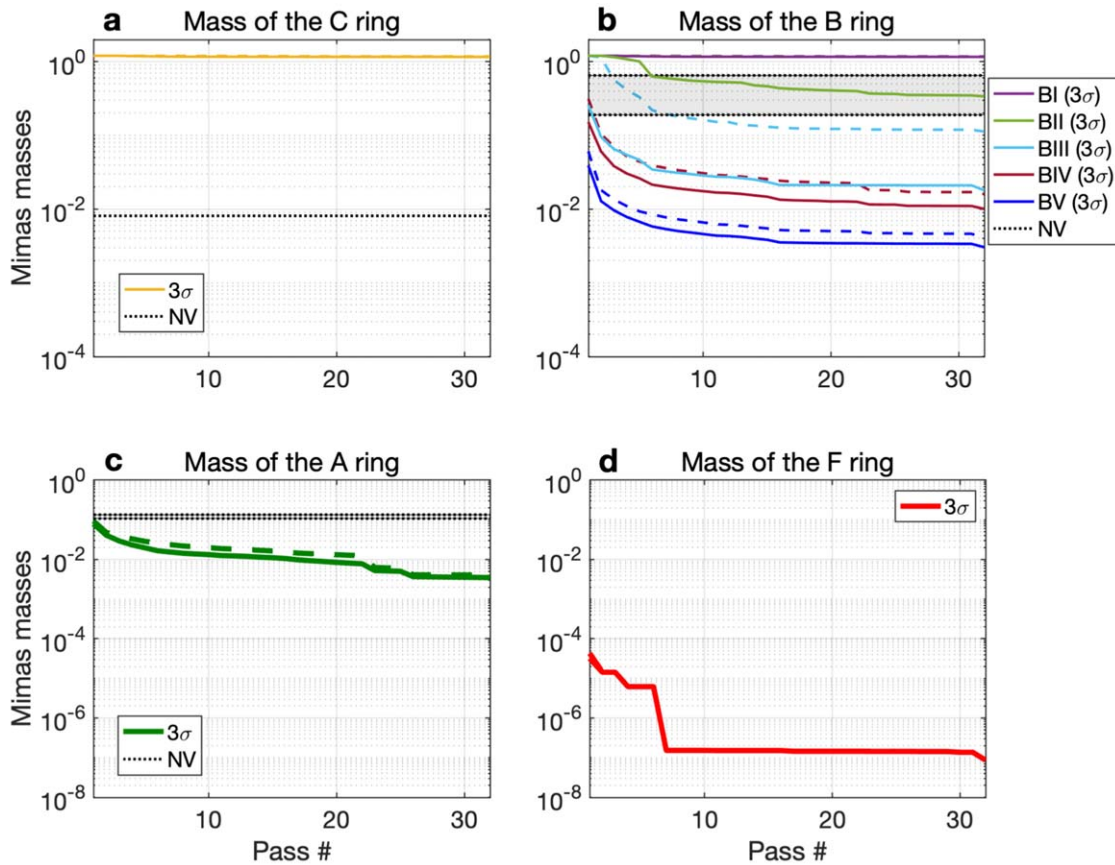


Figure 9. Equivalent of Figure 5 for Scenario 2.

variants of the Skimmer trajectory. As mentioned earlier, for Scenario 2 the results are compared with Scenario 1 once after 21 passes (indicated by *), in order to study the effect of lower ring altitudes, and once after all 32 passes, to study the effect of a larger number of flybys.

We now discuss the effect on the retrieval of the ring and moon masses, as well as Saturn’s k_{22} , of including additional parameters in the solved-for vector (as reported in Table 2), which are not the focus of our study (e.g., the static gravity field of Saturn). Figure 11 shows the correlation coefficients between the estimated parameters of interest (listed in Table 3) and other parameters that can influence the estimation accuracies. We find the highest correlations (0.90–0.95) between the masses of the C ring and the masses of some of the B-ring regions. This can happen both because of the proximity of these regions to each other, as well as the relatively high spacecraft altitudes during the overflights, for both scenarios. In fact, the correlations drop significantly (<0.5) for the masses of the A and F ring and the other parameters considered, due to the spacecraft proximity and ability to better resolve the radial mass distribution. It would not be efficient to report or plot the correlation coefficients for all the parameters included in the analysis (the correlation matrix is a squared matrix of size 1012 for Scenario 1 and size 1507 for Scenario 2). However, we find that the correlations between the parameters of interest in Table 3 and the remaining parameters (including the state vectors of Prometheus, Pandora, and Mimas), are also all below 50%.

4.3. Mimas Flybys

The equatorial Skimmer trajectory provides numerous opportunities for close targeted flybys of the inner moons of Saturn. Among them, Mimas is a target of particular interest for in-depth gravity field measurements, as Cassini did not collect close gravity measurements of this object. In our simulations, we assume that the spacecraft performs six close flybys of the moon (<100 km altitude) during the ring tour (Figure 12). In order to maximize the spacecraft sensitivity to tidal disturbances of Mimas’s gravity field, we also assume that the flybys are all contained in Mimas’s equatorial plane. The last condition is not required, however it is desirable and achievable by means of trajectory optimization. We are interested in the determination of Mimas’s Love number k_2 , which measures the tidal variations of the gravitational potential in the satellite’s equatorial plane, which depend on the satellite’s orbit eccentricity and mean anomaly (Iess et al. 2012). In addition to the spacecraft’s ground tracks and altitude over the icy surface of Mimas, Figure 12 also shows Mimas’s true anomaly distribution along its orbit. In order to determine the value of k_2 with the desired accuracy, the values of the true anomaly must be spread for a uniform sampling of the tidal cycle. The simulations include one pass close to periapsis (0°) and one pass close to apoapsis (180°) to Saturn. The other passes are close to quadrature ($\pm 90^\circ$).

The results of the estimation of Mimas’s k_2 are summarized in Figure 13, in terms of 3σ uncertainty. In the estimation process, the uncertainty on the state of the satellite is accounted

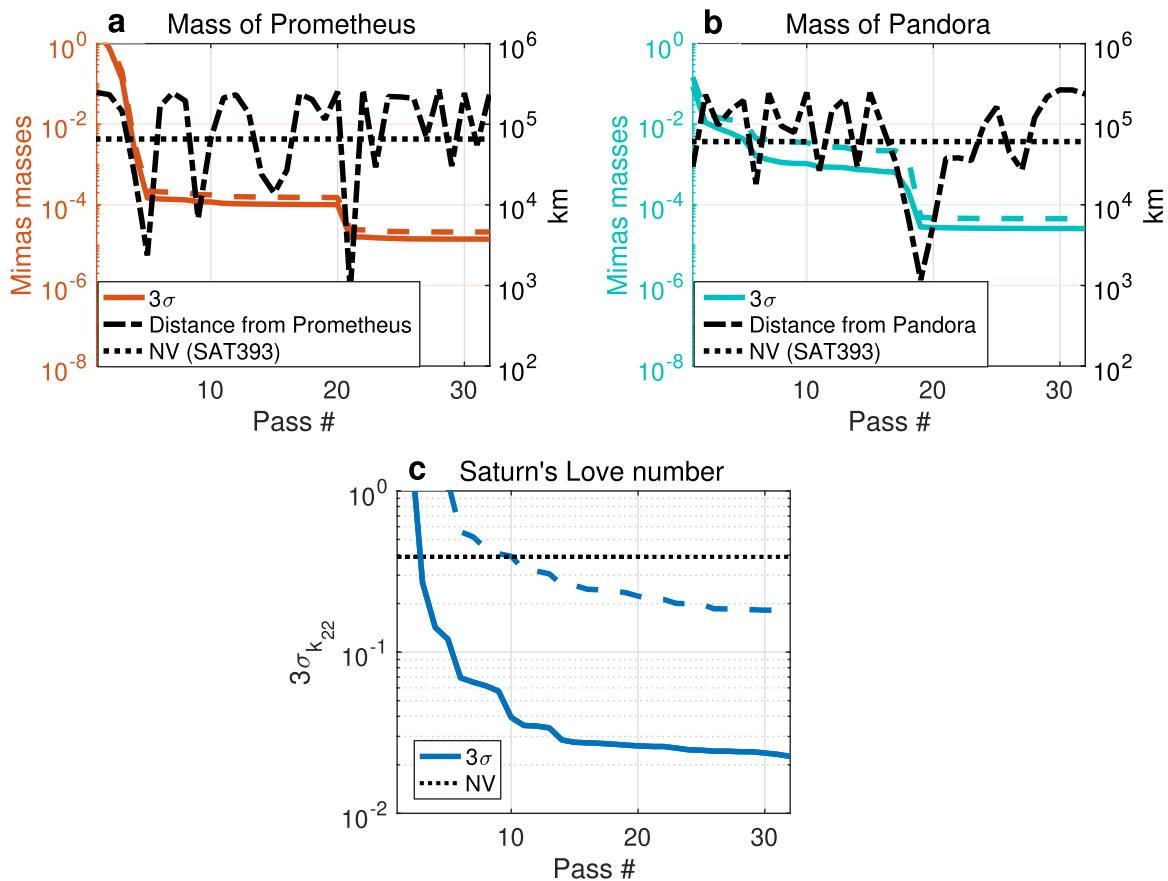


Figure 10. Equivalent of Figure 8 for Scenario 2.

Table 3
Comparison of Main Results from Scenario 1 and 2, in Terms of Predicted 3σ Uncertainties

Estimated Parameter	Nominal Value	Scenario 1 (3σ)		Scenario 2* (3σ)		Scenario 2 (3σ)	
		w/o acc	w acc	w/o acc	w acc	w/o acc	w acc
C mass (Mimas masses)	0.0081 ^a	0.0717	0.1750	1.1580	1.1772	1.1556	1.1724
BI mass (Mimas masses)		0.0276	0.0568	1.1580	1.1772	1.1568	1.1724
BII mass (Mimas masses)		0.0145	0.0287	0.4016	1.1652	0.3380	1.1592
BIII mass (Mimas masses)	0.1892–0.6486 ^b	0.0087	0.0165	0.0211	0.1223	0.0180	0.1126
BIV mass (Mimas masses)		0.0040	0.0089	0.0127	0.0227	0.0101	0.0159
BV mass (Mimas masses)		0.0009	0.0038	0.0034	0.0050	0.0030	0.0041
A mass (Mimas masses)	0.1081–0.1351 ^c	0.0037	0.0052	0.0081	0.0128	0.0035	0.0041
F mass (Mimas masses)	n/a	5.79×10^{-8}	5.91×10^{-8}	1.45×10^{-7}	1.45×10^{-7}	8.63×10^{-8}	8.63×10^{-8}
Prometheus mass (Mimas masses)	4.30×10^{-3d}	1.75×10^{-4}	2.63×10^{-4}	1.59×10^{-5}	2.29×10^{-5}	1.59×10^{-5}	2.08×10^{-5}
Pandora mass (Mimas masses)	3.71×10^{-3d}	5.05×10^{-5}	7.22×10^{-5}	2.70×10^{-5}	4.69×10^{-5}	2.58×10^{-5}	4.53×10^{-5}
Saturn's k_{22}	0.390 ^e	0.027	0.147	0.026	0.214	0.023	0.179

Notes.^a Hedman & Nicholson (2013).^b Hedman & Nicholson (2016).^c Tiscareno et al. (2007).^d Jacobson (2016).^e Lainey et al. (2017).

for by estimating the state vector of Mimas at reference time. Upon completion of the six flybys, the predicted 3σ accuracy for k_2 is 0.012, about 10 times better than the current knowledge of Titan's k_2 (Iess et al. 2012). The estimation of the static gravity field, despite being included in the vector of solved-for parameters, is not discussed in this study. The simulated flybys of Mimas are not optimized for the

determination of the zonal gravity field, due to the poor range of Mimas's latitudes sampled during the equatorial flybys.

5. Discussion and Conclusion

The innovative class of gravity measurements proposed and evaluated in this study allows for the accurate analysis of the

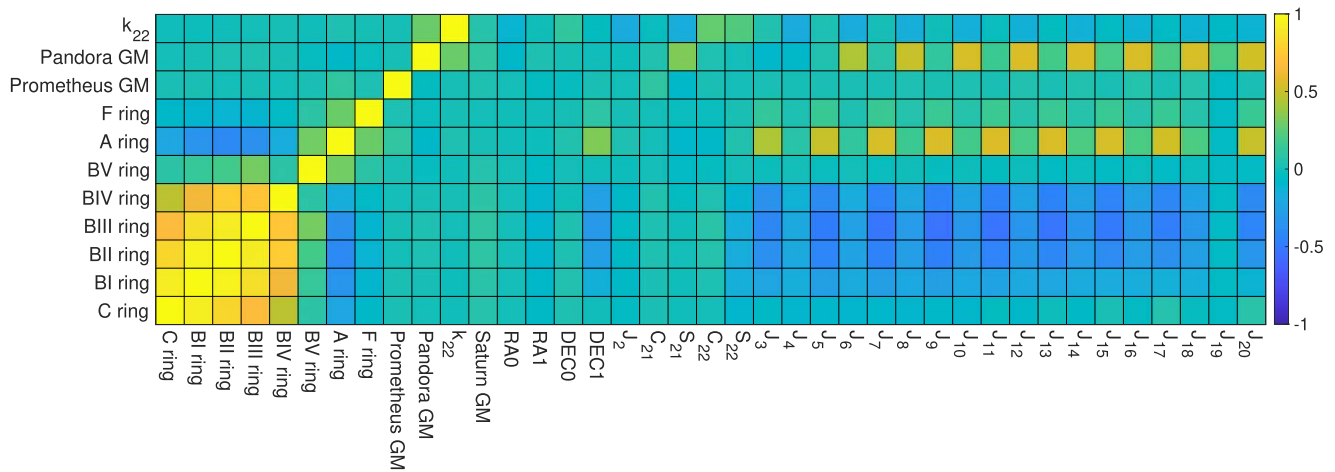


Figure 11. Correlation matrix among the parameters of interest (Table 3, on the vertical axis), as well as with additional gravitational parameters (horizontal axis). Correlations are considered low below 50%.

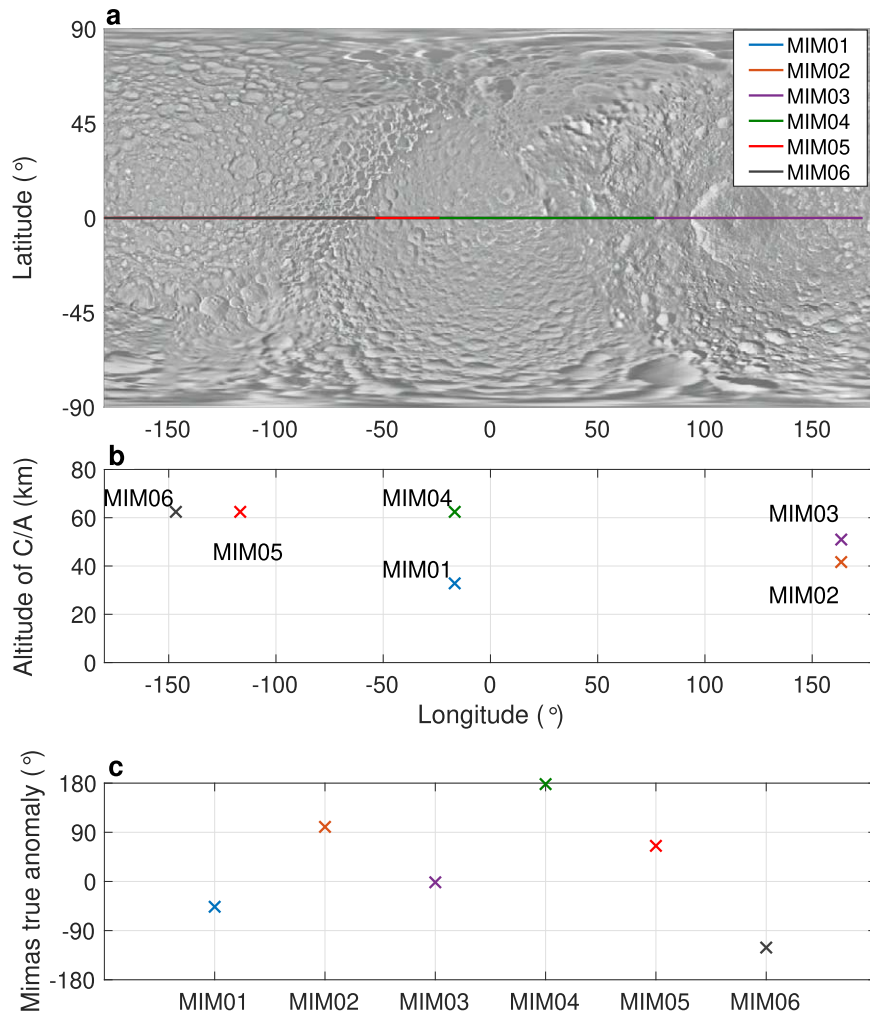


Figure 12. (a) Spacecraft ground tracks during the six close flybys of Mimas (background image credit: NASA/JPL-Caltech/Space Science Institute). (b) Altitude of the flybys as a function of longitude. (c) Mimas’s true anomaly around Saturn as a function of flyby number.

mass distribution throughout Saturn’s inner system. The novel Skimmer concept allows a spacecraft to fly unprecedentedly close to the rings of Saturn, providing a new perspective on the formation and interactions between rings and icy moons. The

combination of the cutting-edge trajectory design and the new-generation radio transponders is key to achieving high accuracies in the determination of the mass, geometry, and position of the ring and satellite system. These spatial and

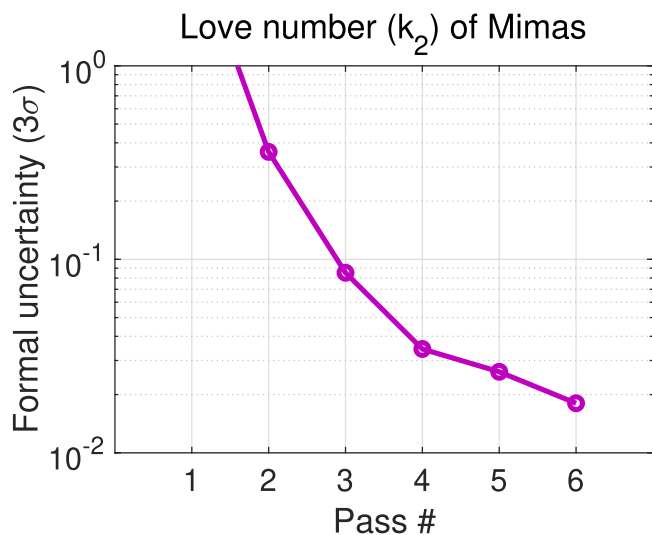


Figure 13. Predicted uncertainty (3σ) for Mimas's Love number (k_2), as a function of flyby number.

temporal maps are crucial for inferring the age of the rings and moons, which in turn provide information about the formation of Saturn and the solar system.

The determination of Mimas's tidal number k_2 is central for the detection of a subsurface ocean underneath the icy surface, as possibly indicated by the magnitude of the measured librations (Tajeddine et al. 2014). The parameter measures the ratio between the perturbed and perturbing potentials (Iess et al. 2012) and represents the elastic response of the satellite to an external forcing. In the presence of a subsurface layer of liquid water, the estimated value must be significantly larger than 0 (perfectly rigid body), but smaller than the theoretical value (1.5) for an incompressible liquid body (Iess et al. 2012). To the best of our knowledge, numerical predictions of Mimas's degree-2 Love number as a function of the satellite's interior structure are not available to date. However, it is possible to reference studies conducted for Europa (Moore & Schubert 2000; Wahr et al. 2006) and Titan (Rappaport et al. 2008), although these moons are considerably larger in size. For reference, the tidal parameter k_2 for a model of Europa that hosts an internal ocean is predicted to be between 0.14 and 0.26 (Moore & Schubert 2000; Wahr et al. 2006). For Titan, which is known to harbor a hidden global ocean, the measured value is between 0.59 and 0.64 (Iess et al. 2012), in comparison to a theoretical prediction of 0.45 (Rappaport et al. 2008).

In this study we have demonstrated that the equatorial nature of the Skimmer trajectory is extremely favorable for sampling Mimas's tidal potential at different mean anomalies, and obtaining an accurate measurement of its Love number with a 3σ uncertainty that is less than 15% the expected central value for icy and rocky bodies. This level of accuracy most likely allows us to distinguish between an oceanless Mimas, where the body is regarded as solid and elastic everywhere, and the presence of a highly deformable layer, such as an ocean. The problem is described in detail in Rappaport et al. (2008). In the former case, the internal tidal stresses induced by Saturn could be compensated by small tidal deformations, implying a small value of k_2 . In the latter case, the presence of a liquid layer would require larger deformations, resulting in a larger k_2 . For Titan, the comparison between these two cases entails a difference in the value of k_2 of about 0.42 (Rappaport et al. 2008), much larger than our predicted accuracy for Mimas's

Love number. The value of the degree-2 Love number would most likely be independent of the ocean depth and vertical extension, but would bear some information about the thickness of the icy surface, instead, with a thicker shell implying a smaller value. Rappaport et al. (2008) report a difference of about 0.06 in Titan's k_2 between an icy crust of only a few kilometers deep and a shell which is 100 km thick. In view of these considerations, a determination of Mimas's Love number with a 3σ accuracy of 0.02 might yield information about the thickness of the outer icy layer, in addition to the detection of a subsurface ocean.

The results obtained in the determination of the masses of the B and F rings are encouraging, as the surface densities of these regions are not as well constrained as the C and A rings from the Cassini mission (Tiscareno et al. 2007; Hedman & Nicholson 2016). The F ring is also thought to host hundreds of small moons whose mass and position are still undetermined, and the Skimmer trajectory allows for the determination of both the azimuthal mean mass of the thin ring, as well as the detection, to a certain extent and with varying accuracy, of local mass concentrations. The comparison between the results from Scenarios 1 and 2 highlights the importance of flying as close as possible to the rings for the determination of their radial density with the desired accuracy, and the improvement in the formal uncertainties is relatively minor after about 20 passes. The only parameters that are better determined in Scenario 2 are the masses of Prometheus and Pandora, due to the random closer encounters with the moons during the ring tour. However, distant flybys of shepherd and icy moons can be maneuvered to occur at closer range regardless of the altitude over the ring plane or number of orbits.

The research described in this paper was carried out at the Jet Propulsion Laboratory, California Institute of Technology, under a contract with the National Aeronautics and Space Administration (80NM0018D0004) (M.P. and M.V.). M.P. and M.V. acknowledge support by the Research and Technology Development (R&TD) program (project #R20258) at the Jet Propulsion Laboratory. ©2022 California Institute of Technology.

ORCID iDs

Marzia Parisi  <https://orcid.org/0000-0003-4064-6634>

References

- Archinal, B. A., Acton, C. H., A'Hearn, M. F., et al. 2018, *CeMDA*, **130**, 22
- Asmar, S. W., Bolton, S. J., Buccino, D. R., et al. 2017, *SSRv*, **213**, 205
- Barbara, J. M., & Esposito, L. W. 2002, *Icar*, **160**, 161
- Charnoz, S., Porco, C. C., Déau, E., et al. 2005, *Sci*, **310**, 1300
- Colwell, J. E., Nicholson, P. D., Tiscareno, M. S., et al. 2009, in *Saturn from Cassini-Huygens*, ed. M. K. Dougherty et al. (Dordrecht: Springer), 375
- Cuzzi, J., Filacchione, G., & Marouf, E. 2018, in *Planetary Ring Systems: Properties, Structure, and Evolution*, ed. M. Tiscareno & C. Murray (Cambridge: Cambridge Univ. Press), 51
- Cuzzi, J. N., & Estrada, P. R. 1998, *Icar*, **132**, 1
- Dermott, S. F., & Thomas, P. C. 1988, *Icar*, **73**, 25
- Durante, D., Parisi, M., Serra, D., et al. 2020, *GeoRL*, **47**, e86572
- Esposito, L. W., Meinke, B. K., Cowell, J. E., Nicholson, P. D., & Hedman, M. M. 2008, *Icar*, **194**, 278
- Estrada, P. R., Durisen, R., & Latter, H. 2018, in *Planetary Ring Systems: Properties, Structure, and Evolution*, ed. M. Tiscareno & C. Murray (Cambridge: Cambridge Univ. Press)
- Estrada, P. R., Durisen, R. H., Cuzzi, J. N., & Morgan, D. A. 2015, *Icar*, **252**, 415
- Evans, S., Taber, W., Drain, T., et al. 2018, *CEAS*, **10**, 79
- Fuller, J. 2014, *Icar*, **242**, 283

- Hedman, M. M., & Nicholson, P. D. 2013, *AJ*, **146**, 12
- Hedman, M. M., & Nicholson, P. D. 2014, *MNRAS*, **444**, 1369
- Hedman, M. M., & Nicholson, P. D. 2016, *Icar*, **279**, 109
- Hedman, M. M., Postberg, F., Hamilton, D., Renner, S., & Hsu, H. 2018, in *Planetary Ring Systems: Properties, Structure, and Evolution*, ed. M. Tiscareno & C. Murray (Cambridge: Cambridge Univ. Press), 307
- Iess, L., Jacobson, R. A., Ducci, M., et al. 2012, *Sci*, **337**, 457
- Iess, L., Militzer, B., Kaspi, Y., et al. 2019, *Sci*, **364**, aat2965
- Iess, L., Stevenson, D. J., Parisi, M., et al. 2014, *Sci*, **344**, 78
- Jacobson 2016, Satellite Ephemerides SAT393, https://naif.jpl.nasa.gov/pub/naif/generic_kernels/spk/satellites/sat393.cmt
- Jacobson 2020, Satellite Ephemerides SAT427, https://naif.jpl.nasa.gov/pub/naif/generic_kernels/spk/satellites/sat427.cmt
- Lainey, V., Casajus, L. G., Fuller, J., et al. 2020, *NatAs*, **4**, 1053
- Lainey, V., Jacobson, R. A., Tajeddine, R., et al. 2017, *Icar*, **281**, 286
- Lass, H., & Blitzer, L. 1983, *CeMec*, **30**, 225
- Mankovich, C. R. 2020, *AGUA*, **1**, e00142
- Mariotti, G., & Tortora, P. 2013, *RaSc*, **48**, 111
- Markham, S., Durante, D., Iess, L., & Stevenson, D. 2020, *PSJ*, **1**, 27
- Marley, M. S., & Porco, C. C. 1993, *Icar*, **106**, 508
- Moore, W. B., & Schubert, G. 2000, *Icar*, **147**, 317
- Murray, C., & French, R. 2018, in *Planetary Ring Systems: Properties, Structure, and Evolution*, ed. M. Tiscareno & C. Murray (Cambridge: Cambridge Univ. Press), 338
- Neveu, M., & Rhoden, A. R. 2017, *Icar*, **296**, 183
- Nimmo, F., Bills, B. G., & Thomas, P. C. 2011, *JGRE*, **116**, E11001
- Notaro, V., Durante, D., & Iess, L. 2019, *P&SS*, **175**, 34
- Parisi, M., Galanti, E., Folkner, W. M., et al. 2020, *JGRE*, **125**, e06416
- Parisi, M., Kaspi, Y., Galanti, E., et al. 2021, *Sci*, **374**, 964
- Park, R. S., Folkner, W. M., Williams, J. G., & Boggs, D. H. 2021, *AJ*, **161**, 105
- Rappaport, N. J., Iess, L., Wahr, J., et al. 2008, *Icar*, **194**, 711
- Roatsch, T., Jaumann, R., Stephan, K., & Thomas, P. C. 2009, in *Saturn from Cassini-Huygens*, ed. M. K. Dougherty et al. (Dordrecht: Springer), 763
- Seal, D. A., & Buffington, B. B. 2009, in *Saturn from Cassini-Huygens*, ed. M. K. Dougherty et al. (Dordrecht: Springer), 725
- Tajeddine, R., Rambaux, N., Lainey, V., et al. 2014, *Sci*, **346**, 322
- Thomas, P. C., Tajeddine, R., Tiscareno, M. S., et al. 2016, *Icar*, **264**, 37
- Tiscareno, M. S., Burns, J. A., Nicholson, P. D., Hedman, M. M., & Porco, C. C. 2007, *Icar*, **189**, 14
- Tiscareno, M. S., Vaquero, M., Hedman, M. M., et al. 2021, *BAAS*, **53**, 372
- Vaquero, M., Senent, J., & Tiscareno, M. S. 2019, in *29th AAS/AIAA Space Flight Mechanics Meeting* (Pasadena, CA: JPL, NASA), 19, <http://hdl.handle.net/2014/50149>
- Wahl, S. M., Parisi, M., Folkner, W. M., et al. 2020, *ApJ*, **891**, 42
- Wahr, J., Zuber, M. T., Smith, D. E., & Lunine, J. I. 2006, *JGRE*, **111**, E12005